Spectroscopic Imaging of Sub-Kilometer Spatial Structure in Lower Tropospheric Water Vapor

David R. Thompson[1], Brian H. Kahn[1], Philip G. Brodrick[1], Matthew D. Lebsock[1], Mark Richardson[1], and Robert O. Green[1]

[1]Jet Propulsion Laboratory, California Institute of Technology, Pasadena, CA 91103 USA

Correspondence: David R. Thompson (david.r.thompson@jpl.nasa.gov)

Abstract. Understanding the subgrid spatial variability of water vapor is important for parameterizing and simulating cloud processes in General Circulation Models (GCMs). This study maps sub-kilometer spatial structures in total atmospheric column water vapor with Visible to Shortwave Infrared (VSWIR) imaging spectroscopy. We describe our inversion approach and validate its accuracy with coincident measurements by airborne imaging spectrometers and the AERONET ground-based observation network. Next, data from NASA's AVIRIS-NG spectrometer enables the highest resolution measurement to date of water vapor's spatial variability and scaling properties. We find second order structure function scaling exponents consistent with prior studies of convective atmospheres. Finally, we conclude by discussing the implications of these measurements and paths toward future campaigns to build upon these results.

1 Introduction

Tropospheric water-vapor is highly variable in space and time. Clouds and precipitation structures are embedded within complex spatial distributions of water vapor that have important consequences for parameterization of moist atmospheric processes in General Circulation Models (GCMs). The dynamic relationship between water vapor sources, sinks, and atmospheric mixing leads to highly variable humidity at the sub-grid scale. Understanding this variability, and how it couples to a myriad of cloud types and multi-scale organization, is key for advancing the parameterization and simulating cloud processes in GCMs. To this end, *structure functions* describe change in the vapor field as a function of distance, quantifying its spatial texture across scales. They are used to analyze many atmospheric components including temperature, winds, trace gas concentrations, and water vapor (Nastrom et al., 1986; Cho et al., 1999). Structure functions can indicate the recent history of the air mass. They can distinguish convective and non-convective systems (Selz et al., 2017), and indicate precipitation rates embedded within a moist column of air with variable levels of column water vapor (Edwards et al., 2019).

For a one-dimensional field $f(i)$ indexed by location i, the nth order structure function $S_n(r)$ is defined as:

$$S_n(r) = E\big[\, |f(i+r) - f(i)|^n \,\big] \tag{1}$$

where r is a separation distance between pairs of points, and E is the expectation over locations. More generally, $S_n(r)$ can represent variability along one direction of a multidimensional field. At least one study of water vapor data has found minor differences in satellite cross-track and along-track directions (Pressel and Collins, 2012), but in general water vapor variability

25   is considered horizontally isotropic. $S_n(r)$ is estimated using the mean of observed water vapor values at different spatial offsets. Over a restricted range of distances, structure functions can be described with a power law:

$$S_n(r) \propto r^{\zeta_n} \qquad (2)$$

where ζ_n is the *scaling exponent* of order n. The scaling exponent of order two is related to the commonly-used Fourier power spectrum exponent β:

$$\beta = -(\zeta_2 + 1) \qquad (3)$$

These values can diagnose specific atmospheric transport processes. Following Kolmogorov theory, a passive tracer in turbu-

30   lence has a theoretical second-order scaling exponent ζ_2 of 2/3, or equivalently, a Fourier power spectrum exponent β of -5/3 (Pope, 2001).

     Previous studies have used a range of instruments to measure water vapor structure functions. In situ aircraft sensors measure a one-dimensional time series along the aircraft flight track. Nastrom et al. (1986) measured separation distances from 150 to 1500 km using this technique. They found ζ_2 ranging from the theoretical value of 2/3 to unity. Later Cho et al. (1999) found

35   ζ_2 consistent with 2/3 over distances of multiple kilometers. These surveys have recently been augmented by airborne LiDAR measurements, which provide vertical profiles along the flight track. A series of LiDAR observations by Fischer et al. (2012, 2013) measured airmasses at scales down to 2 km. They reported $\zeta_2 = 0.6 - 0.75$ in convective airmasses, and $\zeta_2 = 1.0 - 1.2$ in non-convective airmasses. Convective environments had shallower scaling indicating higher spatial variability at small scales. They hypothesized that this flatter power spectrum slope, which was also common in boundary layer airmasses, was related to

40   the small-scale injection of water vapor anomalies by convective eddies. However, their study did not conclusively identify the cause. More recently, Selz et al. (2017) compared airborne LiDAR measurements with simulations at scales above 11 km. This study confirmed that power law exponents were strongly related to altitude and the presence or absence of convection. They showed ζ_2 above 1 for nonconvective airmasses in the free troposphere, near 0.6 in the boundary layer, and as low as 0.2 in convective airmasses.

45   Contrasting with localized, high resolution aircraft data, orbital data such as the Atmospheric Infrared Sounder (AIRS) on EOS Aqua have provided more comprehensive power law exponents across the mesoscale and synoptic scales, but without resolving features smaller than typical GCM grids of 100 km. Kahn and Teixeira (2009) developed a global climatology of scaling properties between 150-1200 km based on vertically-resolved temperature (T) and specific humidity (q) observations by AIRS. Kahn et al. (2011) extended these results and compared them to climate GCMs, MERRA reanalysis, and VOCALS-REx

50   in situ observations of vertically-resolved T and q within and above shallow cumulus off of the coast of Peru. They found strong evidence of $\zeta_2 = 2/3$ scaling in the boundary layer and tropopause at all latitudes, with steeper scaling in the mid-troposphere and at low latitudes. This was consistent with the view of water vapor as a passive scalar in turbulent flow, and implied more

small-scale variability than was predicted by contemporaneous GCMs. This increased scaling of the tropical free troposphere
was also consistent with theoretical predictions of steeper scaling of column water vapor within and near strongly precipitating
55 convection (Edwards et al., 2019). Interestingly, their analysis of aircraft data from the VOCALS-REx experiment suggested a
steepening of the curve at the smallest scales below 10 km (Kahn et al., 2011). This result suggested a possible change in the
scaling properties at the finest resolutions.

These studies contribute to a growing body of literature on water vapor scaling. However, important gaps remain. High
spatial resolution data are sparse, and most studies explore spatial scales above 1 km. To our knowledge no study has yet
60 corroborated the Kahn et al. (2011) steepening phenomenon at scales less than 10 km, or probed the structure functions at
scales less than 2 km. Most aircraft data consist of one dimensional time series, rather than the two-dimensional maps available
from instruments like AIRS. Thus, at the finest scales, small sample sizes can increase uncertainty in the derived exponents
(Selz et al., 2017; Guillaume et al., 2018).

A new generation of orbital instrumentation may shed new light on fine-scale water vapor. Visible to Shortwave Infrared
65 (VSWIR) imaging spectrometers, such as NASA's upcoming EMIT mission (Green et al., 2019) or the expected Surface
Biology and Geology (SBG) investigation (National Academies of Sciences and Medicine, 2018), are highly sensitive to the
water vapor column absorption (Shivers et al., 2019). They typically have a spectral resolution of 5-10 nm and span the
380 - 2500 nm interval, a range which overlaps significant water absorption features. A typical pushbroom instrument could
have as many as 1200 cross-track measurements with ground sampling distances of 30-60 m. Most such investigations target
70 surface properties. However, a byproduct of this analysis will be accurate column-averaged water vapor measurements at
high spatial resolution over wide areas. The spatial resolution and accuracy of the derived water vapor column measurements
will be unprecedented, providing opportunities to probe the horizontal variability of water vapor on global scales. Before
these missions launch, archives of airborne precursor data provide an opportunity to validate the technique and begin the
investigation.

75 This manuscript demonstrates direct mapping of the sub-kilometer spatial structure in column water vapor using an airborne
VSWIR imaging spectrometer. We first describe our model for vapor absorption features in the near- to shortwave infrared. We
estimate clear-sky vapor concentrations by inverting a combined model of the atmosphere and surface reflectance after filtering
out cloud-affected footprints. We validate the approach with NASA's "Classic" Airborne Visible Infrared Imaging Spectrome-
ter, AVIRIS-C (Green et al., 1998), evaluating overflights of the AERONET observation network (Holben et al., 1998). Finally,
80 we analyze imaging spectroscopy data acquired during the "Next Generation" Airborne Visible Infrared Imaging Spectrometer
(AVIRIS-NG) India campaign of 2018. This campaign includes several scenes with highly favorable solar geometry, provid-
ing a uniquely high resolution measurement of the H_2O vapor column. This enables estimation of the H_2O spatial structure
functions at sub-kilometer scales. We find confirming evidence of $\zeta_2 = 2/3$ scaling in some but not all atmospheres, with Kahn
et al. (2011) curve steepening that continues down to at least 100 m. We conclude by discussing the implications of these
85 measurements and paths toward future campaigns that could build upon the results.

2 Methods

2.1 Atmospheric Model

Our technique estimates water vapor independently for each spatial location by inverting an atmospheric radiative transfer model. We define a state vector $\boldsymbol{x}$ containing all the free parameters in the system. It includes the surface reflectance vector

90 ρ, the column water vapor concentration q_v, and the aerosol optical depth at 550 nm. Aerosol optical properties were derived from a canonical sulfate aerosol type and validated in prior studies of the India campaign (Thompson et al., 2019). A *forward model* $\boldsymbol{F}(\boldsymbol{x})$ maps this state onto an observed radiance at the sensor, $\boldsymbol{L}_o$:

$$\boldsymbol{L}_o \quad = \quad \boldsymbol{F}(\boldsymbol{x}) + \boldsymbol{\epsilon} \tag{4}$$

Boldface represents a vector or matrix, e.g. $\boldsymbol{L}_o$ has one element for each spectrometer channel. The random variable $\boldsymbol{\epsilon}$ represents instrument noise, distributed according to a zero-mean Gaussian with covariance $\boldsymbol{\Sigma}_e$. We can decompose $\boldsymbol{L}_o$ into different

95 photon paths, with ∘ representing element-wise multiplication:

$$\boldsymbol{L}_o \quad = \quad \boldsymbol{L}_{atm} \quad + \quad \boldsymbol{t} \circ \boldsymbol{L}_{dn} \circ \frac{\boldsymbol{\rho}}{1 - \boldsymbol{S} \circ \boldsymbol{\rho}} \quad + \quad \boldsymbol{\epsilon} \tag{5}$$

Here $\boldsymbol{L}_{atm}$ represents the *path radiance* caused by molecular and particle scattering; these photons never reach the surface. The second term represents all the photons that interact with the surface at least once. $\boldsymbol{L}_{dn}$ is the downwelling illumination at the bottom of the atmosphere. $\boldsymbol{\rho}$ is the spectral surface reflectance. $\boldsymbol{t}$ is the atmospheric transmittance from the surface to the sensor along its line of sight. $\boldsymbol{S}$ is the spherical sky albedo observed from the ground. The relation in Equation 5 holds for a

100 locally-homogeneous and Lambertian surface, but small departures from these conditions are not catastrophic and in any case the assumptions hold sufficiently well for the scenes in this study.

Our atmospheric model calculates the optical coefficients $\boldsymbol{L}_{atm}$, $\boldsymbol{t}$, and $\boldsymbol{S}$ using the MODTRAN 6.0 software package (Berk and Hawes, 2017). Specifically, we use the DISORT code with 8-stream multiple scattering calculations. The absorption model uses a correlated-k representation with 0.1 cm^{-1} bins. Vertical profiles are assigned from a 20-layer stratified atmosphere.

105 For computational efficiency, we do not run the complete RTM for each evaluation of $\boldsymbol{F}(\boldsymbol{x})$. Instead, we calculate optical coefficients in advance to fill a lookup table for each component in the right side of equation 5, and then interpolate within this table to determine the precise radiance for any given state vector. Figure 1 illustrates the atmospheric transmittance in the measurement interval from 380-2500 nm, including several prominent absorption features related to H$_2$O rovibrational overtones. Absorption features at 940 and 1140 nm carry most of the water column information. Stronger features at 1380 and

110 1880 nm are saturated at atmospheric path lengths, and consequently less useful.

The remote H$_2$O measurements aim to quantify the integrated mass of water vapor directly above each pixel in the scene. However, this is not always possible for a solar-reflected signal. Neglecting scattering, which is small in the near infrared, the remote water vapor observation measures absorption along a two-part optical path from the sun to the ground to the sensor. The sun is seldom directly overhead, and its downwelling illumination enters the atmosphere at some horizontal offset from

115 the reflection point (Figure 1, Right). Consequently, a spectrum's spatial sensitivity can extend far beyond the target pixel
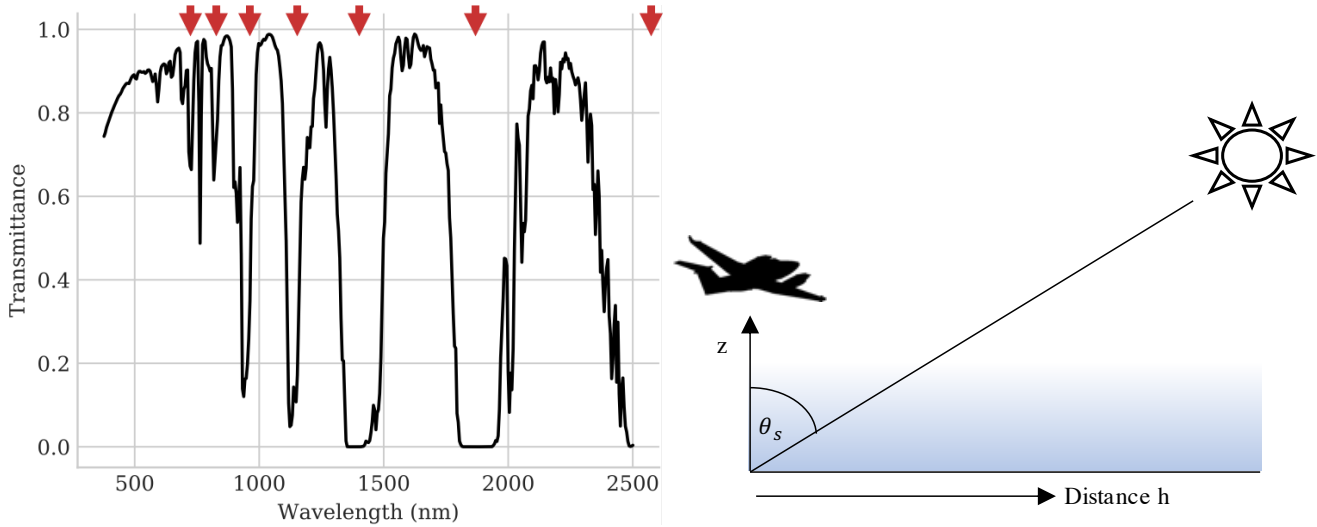
Figure 1. Left: Atmospheric transmissivity from 380-2500 nm reveals multiple H_2O absorption features, indicated with gray arrows. Right: The spatial sensitivity of solar-reflected measurements depends on water vapor absorption along the optical path from the sun to the ground to the sensor. Aircraft image credit: NASA

in the direction of the sun. Projected onto the ground, the vapor absorption path forms a long, thin footprint that extends tens or hundreds of meters from the target pixel in the sunward direction. To quantify this effect, we define the water vapor spatial sensitivity as the extinction-weighted distance between downwelling and upwelling beams. We use $g(h)$ to represent the relative sensitivity to water vapor at h, some horizontal offset distance in the solar direction. For a nadir-pointed observation, assuming that the vertical profile of water vapor is locally constant, the relationship is:

$$
g(h) = \begin{cases} \int_{z\in[z_s,z_o]} \kappa(z)\, dz & \text{if } h = 0 \\[2mm] \kappa\left(\frac{h}{\tan\theta_s} + z_s\right) \frac{1}{\cos\theta_s} & \text{if } h > 0 \end{cases}
\tag{6}
$$

where $\kappa(z)$ is the water vapor number density at altitude z. The variables z_s and z_o represent the surface elevation and sensor altitude respectively. The spatial sensitivity is strongly dependent on solar zenith angle (θ_s). It is also dependent to some extent on the view angle; if the observation is off-nadir, $g(h)$ includes the sensitivity of both upward and downward paths. We define the average spatial offset of a measurement, μ_h, as the mean horizontal position of the water vapor along the two-part optical path:

$$
\mu_h = \frac{\int_0^\infty h\, g(h)\, dh}{\int_0^\infty g(h)\, dh}
\tag{7}
$$

In addition to shifting the center of the spatial response, larger solar zenith angles can coarsen the effective spatial resolution by stretching the water vapor sensitivity footprint in the sunward direction. We define the effective spatial resolution, R_e, as the symmetric horizontal distance from the center point which encloses 68.2% of the spatial response. This would be equivalent to
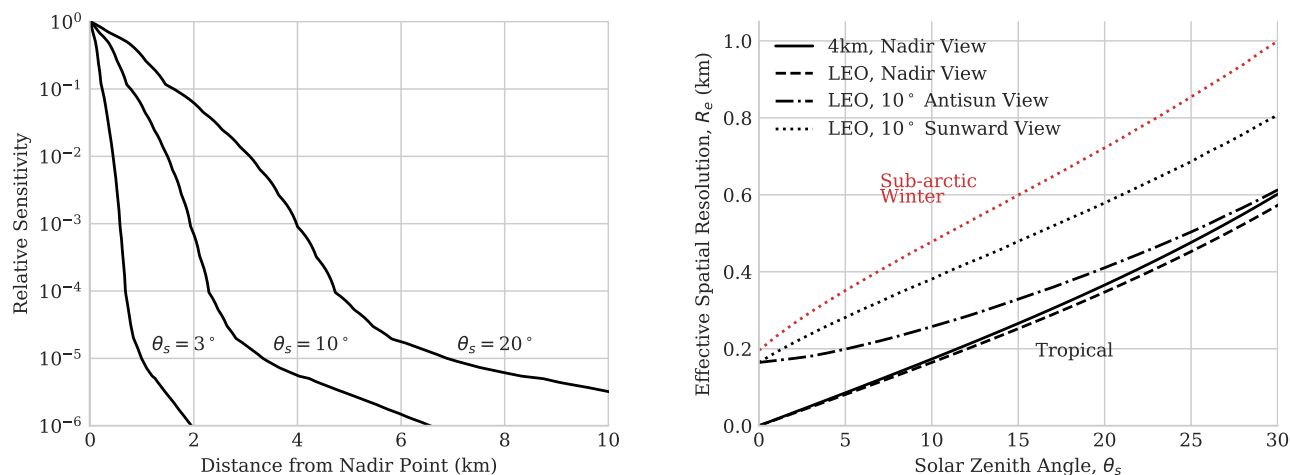
Figure 2. Left: the relative sensitivity to water vapor at 4 km acquisition altitude in a tropical atmosphere as a function of horizontal distance from nadir, partitioned by solar zenith angle θ_s. Right: the effective spatial resolution as a function of solar zenith angle θ_s, at both 4 km and low earth orbit (LEO) acquisition altitudes. The red line shows a sub-arctic winter atmospheric profile indicating the range of spatial resolution across two very different atmospheric conditions. In reality the sun never reaches low zenith angles in polar regions of the globe.

the area inside a single standard deviation if the response function were Gaussian.

$$0.682 = \frac{\int_{\mu_h - R_e}^{\mu_h + R_e} g(h) \, dh}{\int_0^\infty g(h) \, dh} \tag{8}$$

130 Note that the spatial footprint projected on the ground is not radially symmetric; it is long and thin, but retains the native spatial resolution along its short axis. The left panel of Figure 2 shows the relative sensitivity to water vapor at different horizontal offsets for a nadir-viewing measurement of a tropical atmosphere at 4 km acquisition altitude, similar to the observing geometry of the following experiments. We show the response areas for three solar zenith angles. As the solar angles increase, the response function extends farther from the target pixel, with increasingly "thick tails" caused by water absorption along the

135 slanted downwelling path. The right panel of Figure 2 shows the resulting resolutions as a function of solar zenith angle at different viewing geometries and atmospheric profiles, at sensor altitudes of 4 km and Low Earth Orbit (LEO). It shows that the spatial sensitivity is only weakly dependent on the sensor altitude, and somewhat dependent on the viewing angle and the vertical profile of water vapor in the atmosphere. The solar zenith angle is the dominant influence on spatial resolution, motivating a careful selection of flightlines for the following experiments.

140 **2.2 Inversion methodology**

To estimate q_v, we invert a combined model of surface and atmosphere. We use a Bayesian Maximum A Posteriori formalism (Rodgers, 2000) that is common among atmospheric sounding missions. Recent work extended this approach to the Visible-

Shortwave Infrared spectral interval (Thompson et al., 2018b, 2019). The solar-reflected regime is strongly influenced by variability in surface reflectance. Consequently, we fit atmospheric parameters simultaneously with a flexible surface model. As
145 described in Section 2.1, our state vector x includes surface reflectance in every channel, the column water vapor concentration q_v, and the aerosol optical depth at 550 nm. A forward model $F(x)$ transforms this state vector into a simulated radiance at the sensor following Equation 5.

Our inversion determines the most likely state vector to explain the observation L_o. It includes background knowledge with a multivariate Gaussian prior over state vector elements, with mean μ_a and covariance Σ_a. We fit this distribution as in
150 (Thompson et al., 2019), with a library of diverse reflectance spectra. Shrinkage regularization (Theiler, 2012) ensures that the inversion can represent spectra not spanned by original library subspace. The inversion balances this prior against the measurement noise in Equation 5, which is determined from a component-wise instrument performance model (Thompson et al., 2020). The optimal state vector minimizes the following cost function:

$$\chi(x) = (F(x) - L_o)^T \Sigma_e^{-1} (F(x) - L_o) + (x - \mu_a)^T \Sigma_a^{-1} (x - \mu_a) \tag{9}$$

where Σ_e is the instrument noise. This cost is proportional to the negative logarithm of the posterior probability, a product of
155 multivariate Gaussian prior and likelihood terms. We solve it with a trust region gradient descent optimization. In principle, any gradient based optimization would suffice with an appropriate starting point. The inversion typically converges in 10-20 iterations.

2.3 Postprocessing and structure functions

Before analyzing the spatial structure of the resulting H$_2$O maps, we perform several postprocessing steps to improve the
160 map consistency. Even a highly accurate retrieval is likely to suffer some biases due to the influence of the surface type or magnitude. For example, very slight errors in atmospheric path radiance estimates are proportionally larger for dark targets, which can induce a spurious dependence between albedo and water vapor. Surface reflectance features that overlap water vapor absorptions can also influence retrievals. Finally, minor differences in the radiometric response or linearity of different cross-track elements can create striping artifacts in derived products. We address all of these issues with a single empirical
165 correction. We first define a grid of locations $i \in \mathcal{L}$ where the retrieval is performed. We assert that the retrieved water vapor at each location i, written $\hat{q}_i$, is the combination of an underlying "true" water vapor signal q_i, zero-mean measurement noise ϵ_q, and non-stochastic interference by surface and systematic instrument effects. We define a feature vector ψ_i to include the surface reflectance in each channel, and a sparse position vector p encoding the associated cross-track position on the Focal Plane Array (FPA) in a stacked binary representation. The position encoding enables the model to represent radiometric
170 sensitivity of different FPA elements. The column vector ψ_i thus combines ρ_i and p_i. For simplicity, we assume the surface interference is a linear combination of these features, weighted by coefficients ϕ:

$$\hat{q}_i = q_i + \phi^T \psi_i + \epsilon_q \tag{10}$$

To estimate ϕ, we treat the true water vapor component as a random variable. Over large spatial scales, biases due to diverse content will tend to average out, and the sample mean of retrieved values can be used to approximate the true mean. Rearranging

algebraically, we define the local vapor anomaly $\mathcal{A}_i$ as:

$$\mathcal{A}_i = \hat{q}_i - \left[\frac{1}{|\mathcal{L}|} \sum_{j \in \mathcal{L}} \hat{q}_j \right] = \boldsymbol{\phi}^T \boldsymbol{\psi}_i + \epsilon_w \tag{11}$$

175   Where ϵ_w now incorporates variability due to retrieval noise as well as variability in the true water vapor field. Since ϵ_w is zero mean, Equation 11 reduces to a straightforward linear regression problem. For a data matrix $\boldsymbol{U}$ with rows made up of all reflectance spectra, and a vector $\mathcal{A}$ of anomaly values, we estimate ϕ with ordinary least squares regression. We subtract the predicted error from the original estimate to yield the bias-corrected estimate $q_i^{'}$:

$$q'_i = \hat{q}_i - \hat{\boldsymbol{\phi}}^T \boldsymbol{\psi}_i \quad \text{for} \quad \hat{\boldsymbol{\phi}} = \boldsymbol{U}(\boldsymbol{U}^T\boldsymbol{U})^{-1}\boldsymbol{U}^T\mathcal{A} \tag{12}$$

To apply the bias correction, we segment long flightlines into segments of no longer than 2000 pixels each, and apply the
180   interference correction to each segment independently.

A final postprocessing operation smooths each water vapor image with a Gaussian spatial filter. This dramatically reduces the retrieval noise, making it possible to resolve much finer structures. This noise reduction is also beneficial for estimating structure functions, which are bounded artificially on the low end by the average squared noise in neighboring pixels. We use leave one out cross-validation (Shao, 1993) to select an optimal blurring kernel width. To score a candidate width, we compare
185   every point in the scene to the prediction made by applying the blurring kernel to that location, excluding the point under test with appropriate renormalization. The optimal kernel standard deviations range from 4 to 6 in different scenes; we use the lower value to preserve fine spatial structure at sub-100m scales.

After these postprocessing steps, we calculate empirical structure functions for each pixel shift distance d, computing the squared differences between image locations shifted in the along-track direction. Recall that the long flightlines are corrected
190   in parts no longer than 2000 pixels in length, revealing structure functions up to 4 km. To avoid minor offsets in the vapor field on each side of a border, we do not permit shifts across multiple segments. We aggregate the statistics of all segments to form a structure function estimate for each flightline. We manually mask any visible artifacts in water vapor images to exclude them from the calculation. These artifacts are primarily due to the presence of clouds or their shadows. Clouds can also disrupt their local light fields with scattered illumination, an effect visible in water vapor maps as obvious halos around clouds and their
195   shadows. To mitigate this effect, we dilate the masks by 200 m in all directions.

3   Results: AERONET Overflights

We first assess the absolute accuracy of water vapor absorption measurements using airborne overflights of the AERONET robotic observation network (Holben et al., 1998). The AERONET sunphotometers view the sun directly, estimating water vapor by solar extinction (Pérez-Ramírez et al., 2014). Consequently, they do not measure the same optical path as the
200   downlooking sensor. Nevertheless, these coincident overflights validate the approach and provide a ceiling for unmodeled uncertainties. The airborne instrument is AVIRIS-C (Green et al., 1998). It flew on an ER-2 aircraft at approximately 20 km altitude. Our dataset spans six years of operations over California, from 2013-2019, during which it overflew active terrestrial

AERONET sites on over 100 occasions. Our atmospheric model for these observations used an AFGL midlatitude summer profile (Anderson et al., 1986). Aerosols were light throughout the overflights, so we omitted them from the state vector.

205   We use several filtering methods to remove uncertain datapoints. Many overflights are contaminated by clouds. Our comparison excludes obvious clouds recognized by an estimated surface reflectance at 450 nm above 0.2. However, even when opaque clouds do not directly cover the aeronet location, high-altitude cirrus, cloud shadows or scattered irradiance can contaminate a retrieval. Additionally, high spatiotemporal variability in water vapor can cause a discrepancy; it would aggravate the difference in optical paths, as well as the imperfect temporal coincidence between the AERONET acquisitions and the overflight.

210   Considering the strong influence of θ_s demonstrated in Figure 2, and that θ_s during typical flights often reaches 45 degrees or greater, the ground-based measurement could see a very different vapor field if humidity were not horizontally homogeneous. To address these issues, we remove any datapoints where the in-situ standard deviation in H_2O is larger than 0.1 g cm^{-2}, estimated by comparing the 10 temporally closest acquisitions. After this filtering step, 64 datapoints remain. Some discrepancy in the optical paths remain, which becomes larger for column water vapor in free troposphere than the planetary boundary layer.

215   As neither measurement resolves the detailed vertical profile, it is not possible to distinguish these cases without additional information.

Figure 3 compares the AERONET and remote retrievals for all sites. Error bars indicate the variability in water vapor over the 10 closest timesteps (AERONET) or the 10x10 enclosing rectangle of pixels (AVIRIS-C). Each AERONET timestep is approximately 5 minutes, so our window provides a measure of variability in the hour around the flight. These overflights

220   represent a wide range of atmospheric conditions and solar angles. They span column water vapor concentrations from approximately 0.3 to 2.5. The airborne and uplooking measurements show strong agreement, with a correlation coefficient R of 0.95. A few AVIRIS-C observations with very high variability are likely clouds or cloud shadows that survived the filtering process. Nevertheless, the result is broadly consistent with AERONET accuracy of 12–15% for column water vapor, a claim which has been validated independently by comparison to microwave radiometers (Pérez-Ramírez et al., 2014). This provides confidence

225   in the accuracy of the water vapor retrieval. There is a small bias between the two datasets. However, even if we attributed it entirely to the airborne data such an offset would not influence the structure function measurement.

4   Results: Structure Function Measurement

We apply the H_2O retrieval methodology to four flightlines from a 2018 AVIRIS-NG campaign in India. We selected these flightlines for favorable solar observing geometry and because they represented two distinct conditions observed on different

230   days. All flightlines were at 4 km altitude over water, providing a uniform, topographically-flat surface for vapor retrievals. On May 12, two flightlines encountered scattered low clouds. On May 14, two more flightlines encountered clear skies. The solar zenith angles were all less than 10 degrees, providing effective spatial resolutions from 80 to 250 m at nadir. In comparison, the native spatial sampling of AVIRIS-NG at these altitudes was 4 m. In addition to improving spatial resolution, the extreme solar angles also produced significant sunglint, revealing near infrared water features that would otherwise be masked by

235   the absorption of the water surface. Information on each flightline appears in Table 1. We applied the standard AVIRIS-NG
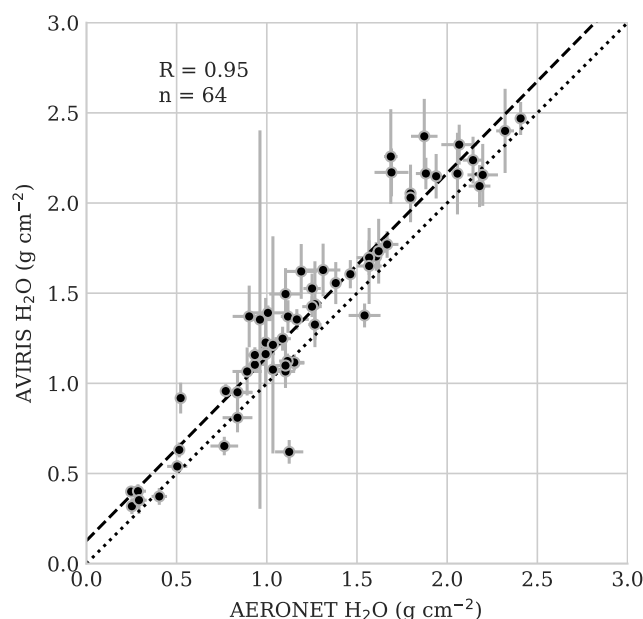
Figure 3. Coincident AVIRIS-C vs AERONET water vapor measurements, filtering out AERONET instances with high temporal variability ($1\sigma > 0.1$ g cm^{-2} over 10 temporally closest measurements).

radiance calibration procedure (Chapman et al., 2019), including corrections to the spectral response function (Thompson et al., 2018a). We then performed water vapor retrievals on all flightlines using a tropical atmospheric profile (Anderson et al., 1986). AVIRIS-NG had a higher intrinsic Signal to Noise Ratio (SNR) than AVIRIS Classic, and the solar angles provided more signal than a typical AERONET overflight from the validation experiment. Consequently, we expected a more sensitive retrieval in 240 the India datasets.

Label	Flightline ID	Date	θ_s	Nadir R_e (m)	Latitude N	Longitude W
A	ang20180512t052609	12 May 2018	9.7	250	21.649	87.775
B	ang20180512t053942	12 May 2018	6.9	177	21.639	87.789
C	ang20180514t055115	14 May 2018	4.1	105	21.524	88.346
D	ang20180514t060206	14 May 2018	3.1	79	21.526	88.325

Table 1. Flightlines used for structure function analysis.

Figure 4 shows a typical spectrum fit. The top panel shows the radiance measurement. The converged model matches the measurement closely, with largest discrepancies in the shortest wavelengths. The middle panel shows the residual error. Some structure at the sub-2% level is consistent with minor model discrepancies or calibration errors. These mostly affect the shortest wavelengths outside the dominant water absorption intervals. The reflectance spectrum in the bottom panel shows a

245   good quality retrieval of a water surface. There is considerable sunglint, a spectrally-flat additive signal that uniformly elevates the spectrum. This raises the near- to shortwave-infrared reflectance, which would normally be zero over liquid water, to values of 12-13%. Elevated reflectance in the presence of sunglint enables high-accuracy retrievals of q_v over open water. This is a reliable consequence of small solar zenith angles under a wide range of wind conditions.

     Figure 5 shows the column water vapor maps for individual segments of the flightlines. In the top panels, dark blue areas

250   indicate manual masks applied to exclude cloudy regions. After the interference correction, the vapor maps are generally free of artifacts except for a minor band at the zero phase angle. This artifact, identified by a white arrow, may be related to pathological effects from the sun glint bidirectional reflectance distribution or the aircraft shadow. It was excluded from the statistics. The smallest-scale variability is almost certainly related to noise in the retrieval algorithm. Larger scale coherent structures show that meaningful differences in water vapor content are resolved at the level of 1-3%, over scales comparable

255   to the predicted spatial resolutions of 80-250 m. The center and bottom panels show example maps for flightlines C and D on May 14, which were entirely free of clouds. In aggregate, the flightlines encountered water vapor values ranging from about 3.23 to 3.42 g cm^{-2}. The smoothing operation dramatically increases the contrast of spatial features (Figure 6).

     Figure 7 shows structure functions for the four flightlines with second order scaling exponents for representative intervals. Grey lines indicate the best-fitting power law exponents over the 500-1000m interval. We also plot the canonical 2/3 slope for

260   reference. The flightlines' configurations of vapor and clouds were all unique, but their scaling functions from the common flight days show similar profiles. This intra-day similarity demonstrates the repeatability of the measurement in a consistent airmass. For flightlines A and B, ζ_2 is 0.64 and 0.63 respectively. These values are very close to the classic 2/3 value of a passive scalar in turbulence. The slope continues to scales well under 1 km, with a steepening of the curve below about 500m. This corroborates the VOCALS-REx data analyzed by Kahn et al. (2011), although those observations were taken in a stable

265   regime within and above stratocumulus clouds off of the coast of S. America. In this case, the observed steepening continues to scales approaching the effective spatial resolution of approximately 250 m. The right panel shows flights C and D on May 14. These flightlines have shallower profiles in the 500-1000 m range, with scaling exponents of 0.41 and 0.29. The curves are less consistent across the two overflights, which might be due to small sample sizes. Flightlines C and D contained just one segment of 2000 m, compared with six segments in each of flightlines A and B.

270   To confirm that the results were robust to slight differences in viewing angles, we recalculated the same result using the central half of the flightline data. This excluded all off-nadir view angles greater than approximately 9 degrees. The results did not change significantly; flightlines A,B,C and D showed ζ_2= 0.55, 0.58, 0.41 and 0.29 respectively. These differences would not be large enough to change our interpretation. In all cases, the maps comprise millions of independent measurements making it possible to resolve structures of magnitudes smaller than the single-pixel noise. All acquisitions, including the

275   extreme shallow scaling of flightlines C and D, are in the range of exponents predicted for convective airmasses by Selz et al. (2017). This is consistent with the presence of convective clouds in the flightlines.
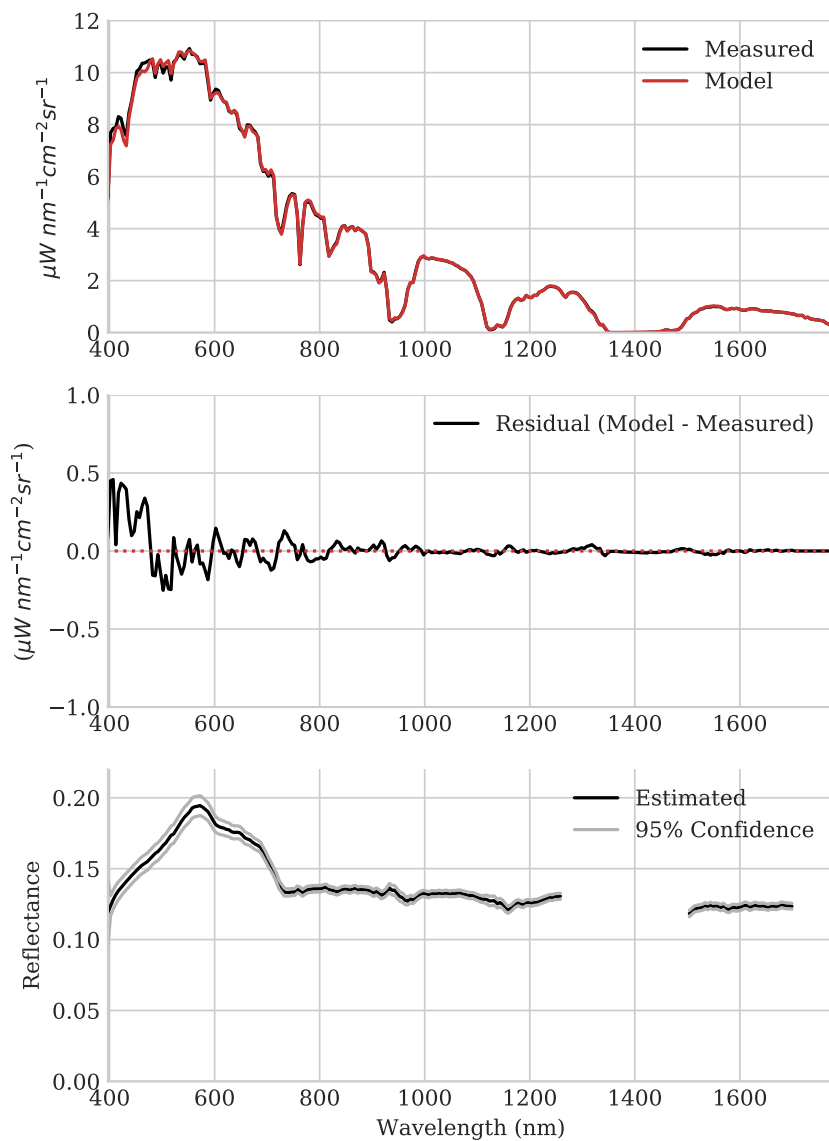
Figure 4. Top: Example radiance spectrum. Middle: Model fit residual. Bottom: Estimated reflectance with 95% confidence bounds.

Column average H$_2$O vapor, flightline A (ang20180514t060206)

1 km   3.25 g cm^{-2} 3.35 g cm^{-2}

Column average H$_2$O vapor, flightline B (ang20180512t053942)

1 km   3.29 g cm^{-2} 3.37 g cm^{-2}

Column average H$_2$O vapor, flightline C (ang20180514t055115)

1 km   3.33 g cm^{-2} 3.42 g cm^{-2}

Column average H$_2$O vapor, flightline D (ang20180514t060206)

1 km   3.23 g cm^{-2} 3.34 g cm^{-2}
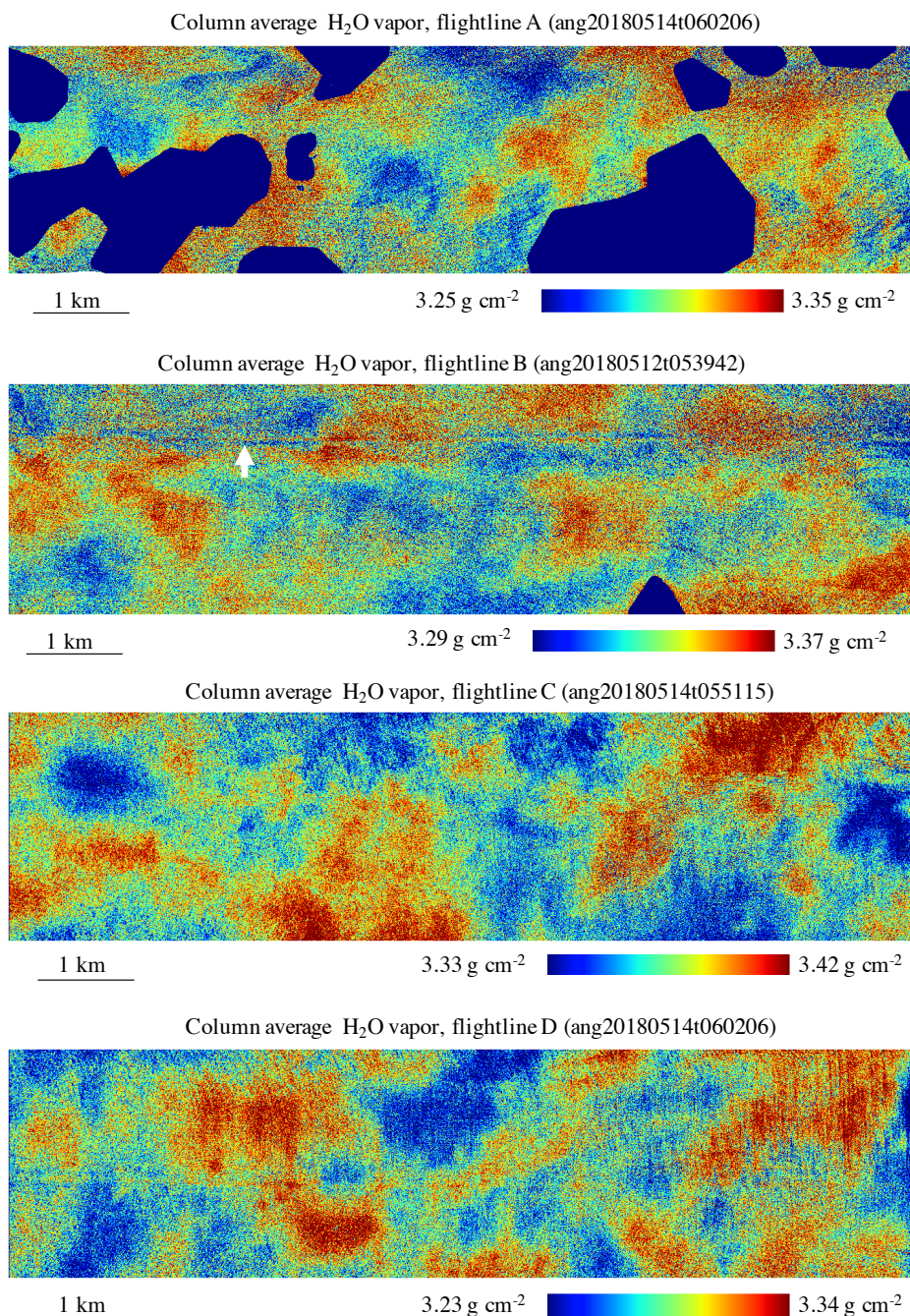
Figure 5. H$_2$O vapor maps. In flightlines A and B, dark blue areas are masked to avoid clouds. A white arrow in indicates an artifact that occurs where the solar phase angle is zero.
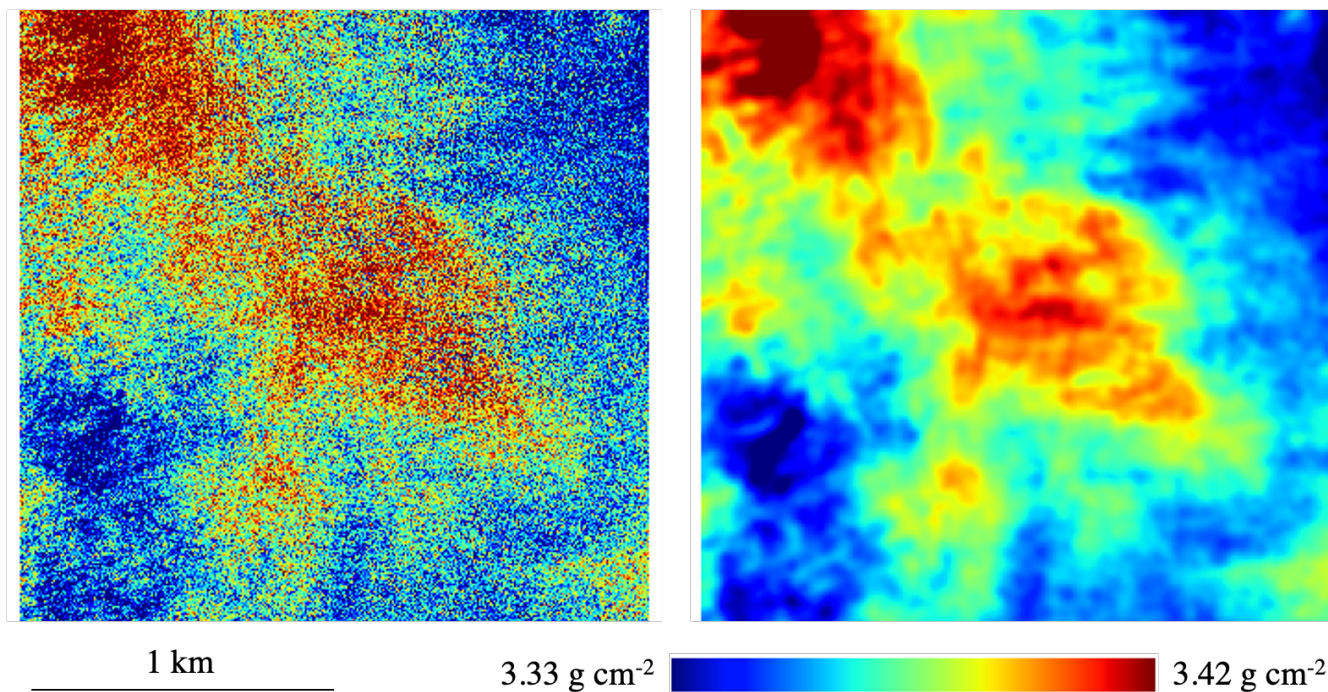
Figure 6. Left: Initial water vapor map from flightine C. Right: Noise reduction after kernel smoothing reveals fine-scale structure at sub-kilometer scales.
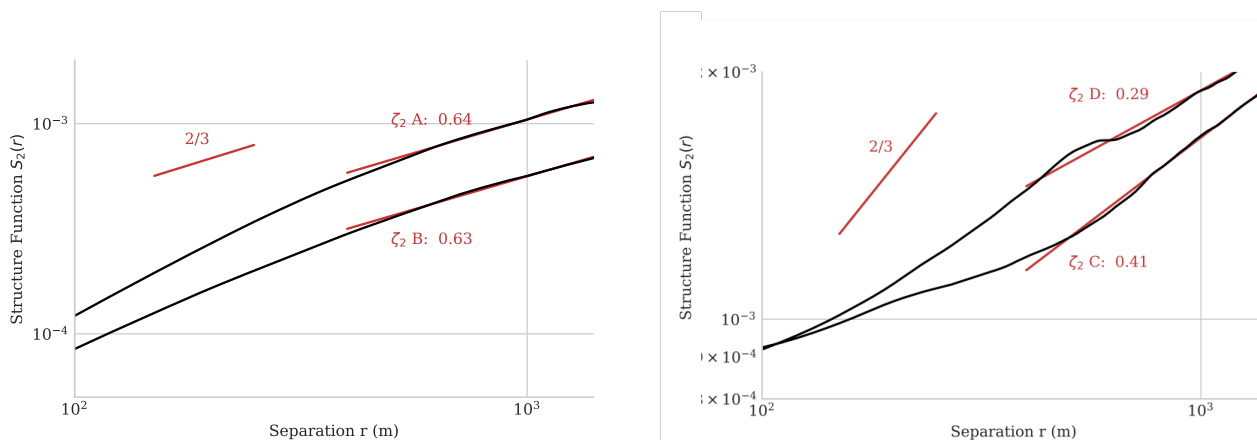
Figure 7. Structure functions for the maps in Figure 5. Left: Flightlines A and B. Right: Flightlines C and D.

5   Conclusion

This paper describes an approach for mapping column-average water vapor at sub-kilometer spatial scales with remote VSWIR imaging spectroscopy. We validate the method by comparison with in-situ AERONET observations. We then map column water vapor using reflected solar sunglint over ocean surfaces in several flightlines from an airborne campaign where favorable solar angles permitted a uniquely high resolution measurement. We find scaling behavior broadly consistent with prior studies, with high repeatability across different observations of the same airmass. The experiment is limited in some respects; for example, it provides only a total-column measurement, making it less compatible with height-resolved structure functions (Kahn et al., 2011). Moreover, stringent requirements on observation geometry limited the dataset to a few representative flightlines. Nevertheless, it provides a proof of concept that VSWIR imaging spectroscopy, primarily used for measurements of surface phenomena, can also provide meaningful, accurate water vapor maps for atmospheric studies.

Future measurement campaigns aiming to observe water vapor with this approach should consider both the solar geometry and signal to noise level, either of which could limit the resolution achievable. In this study, we limited the influence of solar geometry by careful selection of observing conditions. When this is not possible, computer techniques might be used to remove the spatial blurring effect of low solar angles. The effective spatial response function could be calculated and deconvolved from the measured vapor field. Regardless of whether such compensation is possible, the next generation of orbital VSWIR imaging spectrometers should significantly increase the data available for fine-scale mapping of tropospheric water vapor.

Code and data availability.   Code used for the calculations described in this manuscript is available in the ISOFIT code repository under the Apache 2.0 open source license (https://github.com/isofit/isofit). The airborne datasets described in this paper are available from the Jet Propulsion Laboratory (https://aviris.jpl.nasa.gov for AVIRIS-C, and https://avirisng.jpl.nasa.gov for AVIRIS-NG). AERONET data is available from the AERONET web site, (https://aeronet.gsfc.nasa.gov/)

Author contributions.   D. R. Thompson contributed to the writing, algorithm design, experimental concept and execution. P. G. Brodrick contributed to code development, algorithm design and implementation, interpretation of the experiments, and writing. R. O. Green planned, coordinated, and managed the AVIRIS-C and AVIRIS-NG campaigns. B. H. Kahn provided scientific motivation, interpretation of results, and writing. M. D. Lebsock contributed to the measurement concept, data interpretation, and writing. M. Richardson contributed to the measurement concept, code evaluation and validation, and writing.

Competing interests.   The authors have no competing interests with the investigation described in this document.

Acknowledgements. We thank the AERONET station PI(s) and Co-I(s) and their staff for establishing and maintaining the sites used in this investigation. Some of the Cimel Sun-Photometer data was collected by the U.S. Department of Energy as part of the Atmospheric

305 Radiation Measurement Program User Facility (ARM) and processed by the National Aeronautics and Space Administration's Aerosol Robotic Network (AERONET). We thank the members of the AVIRIS-NG team who participated in data acquisition and analysis, including Michael Eastwood, Sven Geier, Mark Helmlinger, Winston Olson-Duvall, and Sarah Lundeen. AVIRIS-NG is sponsored by the National Aeronautics and Space Administration (NASA) Earth Science Division. This research was carried out at the Jet Propulsion Laboratory, California Institute of Technology, under a contract with the National Aeronautics and Space Administration. We also acknowledge the

310 NASA Earth Science Division's AVIRIS-NG instrument and the data analysis program "Utilization of Airborne Visible/Infrared Imaging Spectrometer Next Generation Data from an Airborne Campaign in India" NNH16ZDA001N-AVRSNG. Any use of trade, firm, or product names in this publication is for descriptive purposes only and does not imply endorsement by the U.S. Government. Copyright 2020 California Institute of Technology. Government Sponsorship Acknowledged.

References

315   Anderson, G., Clough, S., Kneizys, F., Chetwynd, J., and Shettle, E.: AFGL atmospheric constituent profiles (0-120 km), Air Force Geophys. Lab. Tech. Report, 86-0110, 1986.

Berk, A. and Hawes, F.: Validation of MODTRAN® 6 and its line-by-line algorithm, Journal of Quantitative Spectroscopy and Radiative Transfer, 203, 542–556, 2017.

Chapman, J. W., Thompson, D. R., Helmlinger, M. C., Bue, B. D., Green, R. O., Eastwood, M. L., Geier, S., Olson-Duvall, W., and Lundeen,
320   S. R.: Spectral and radiometric calibration of the next generation airborne visible infrared spectrometer (AVIRIS-NG), Remote Sensing, 11, 2129, 2019.

Cho, J. Y., Zhu, Y., Newell, R. E., Anderson, B. E., Barrick, J. D., Gregory, G. L., Sachse, G. W., Carroll, M. A., and Albercook, G. M.: Horizontal wavenumber spectra of winds, temperature, and trace gases during the Pacific Exploratory Missions: 1. Climatology, Journal of Geophysical Research: Atmospheres, 104, 5697–5716, 1999.

325   Edwards, T. K., Smith, L. M., and Stechmann, S. N.: Spectra of atmospheric water in precipitating quasi-geostrophic turbulence, Geophysical & Astrophysical Fluid Dynamics, pp. 1–27, 2019.

Fischer, L., Kiemle, C., and Craig, G. C.: Height-resolved variability of midlatitude tropospheric water vapor measured by an airborne lidar, Geophysical research letters, 39, 2012.

Fischer, L., Craig, G. C., and Kiemle, C.: Horizontal structure function and vertical correlation analysis of mesoscale water vapor variability
330   observed by airborne lidar, Journal of Geophysical Research: Atmospheres, 118, 7579–7590, 2013.

Green, R. O., Eastwood, M. L., Sarture, C. M., Chrien, T. G., Aronsson, M., Chippendale, B. J., Faust, J. A., Pavri, B. E., Chovit, C. J., Solis, M., et al.: Imaging spectroscopy and the airborne visible/infrared imaging spectrometer (AVIRIS), Remote sensing of environment, 65, 227–248, 1998.

Green, R. O., Mahowald, N. M., Clark, R. N., Ehlmann, B. L., Ginoux, P. A., Kalashnikova, O. V., Miller, R. L., Painter, T. H., Garcia-Pando,
335   C. P., Realmuto, V. J., et al.: Objectives, Measurements and Data Products of the NASA Earth Surface Mineral Dust Source Investigation, 2019.

Guillaume, A., Kahn, B., Yue, Q., Fetzer, E., Wong, S., Manipon, G., Hua, H., and Wilson, B.: Horizontal and vertical scaling of cloud geometry inferred from CloudSat data, Journal of the Atmospheric Sciences, 75, 2187–2197, 2018.

Holben, B. N., Eck, T. F., Slutsker, I. a., Tanre, D., Buis, J., Setzer, A., Vermote, E., Reagan, J. A., Kaufman, Y., Nakajima, T., et al.:
340   AERONET—A federated instrument network and data archive for aerosol characterization, Remote sensing of environment, 66, 1–16, 1998.

Kahn, B. H. and Teixeira, J.: A global climatology of temperature and water vapor variance scaling from the Atmospheric Infrared Sounder, Journal of climate, 22, 5558–5576, 2009.

Kahn, B. H., Teixeira, J., Fetzer, E. J., Gettelman, A., Hristova-Veleva, S. M., Huang, X., Kochanski, A. K., Köhler, M., Krueger, S. K.,
345   Wood, R., and Zhao, M.: Temperature and Water Vapor Variance Scaling in Global Models: Comparisons to Satellite and Aircraft Data, Journal of the Atmospheric Sciences, 68, 2156–2168, https://doi.org/10.1175/2011JAS3737.1, 2011.

Nastrom, G., Jasperson, W., and Gage, K.: Horizontal spectra of atmospheric tracers measured during the global atmospheric sampling program, Journal of Geophysical Research: Atmospheres, 91, 13 201–13 209, 1986.

National Academies of Sciences, E. and Medicine: Thriving on Our Changing Planet: A Decadal Strategy for Earth Observation
from Space, The National Academies Press, Washington, DC, https://doi.org/10.17226/24938, https://www.nap.edu/catalog/24938/
thriving-on-our-changing-planet-a-decadal-strategy-for-earth, 2018.

Pérez-Ramírez, D., Whiteman, D. N., Smirnov, A., Lyamani, H., Holben, B. N., Pinker, R., Andrade, M., and Alados-Arboledas, L.: Evaluation of AERONET precipitable water vapor versus microwave radiometry, GPS, and radiosondes at ARM sites, Journal of Geophysical
Research: Atmospheres, 119, 9596–9613, 2014.

Pope, S. B.: Turbulent flows, IOP Publishing, 2001.

Pressel, K. G. and Collins, W. D.: First-Order Structure Function Analysis of Statistical Scale Invariance in the AIRS-Observed Water Vapor
Field, Journal of Climate, 25, 5538–5555, https://doi.org/10.1175/JCLI-D-11-00374.1, 2012.

Rodgers, C. D.: Inverse methods for atmospheric sounding: theory and practice, vol. 2, World scientific, 2000.

Selz, T., Fischer, L., and Craig, G. C.: Structure Function Analysis of Water Vapor Simulated with a Convection-Permitting Model and
Comparison to Airborne Lidar Observations, Journal of the Atmospheric Sciences, 74, 1201–1210, 2017.

Shao, J.: Linear model selection by cross-validation, Journal of the American statistical Association, 88, 486–494, 1993.

Shivers, S. W., Roberts, D. A., McFadden, J. P., and Tague, C.: An analysis of atmospheric water vapor variations over a complex agricultural
region using airborne imaging spectrometry, PLOS ONE, 14, 1–28, https://doi.org/10.1371/journal.pone.0226014, https://doi.org/10.1371/
journal.pone.0226014, 2019.

Theiler, J.: The incredible shrinking covariance estimator, Automatic Target Recognition XXII, 8391, 83 910P, 2012.

Thompson, D. R., Boardman, J. W., Eastwood, M. L., Green, R. O., Haag, J. M., Mouroulis, P., and Van Gorp, B.: Imaging spectrometer
stray spectral response: In-flight characterization, correction, and validation, Remote Sensing of Environment, 204, 850–860, 2018a.

Thompson, D. R., Natraj, V., Green, R. O., Helmlinger, M. C., Gao, B.-C., and Eastwood, M. L.: Optimal estimation for imaging spectrometer
atmospheric correction, Remote Sensing of Environment, 216, 355–373, 2018b.

Thompson, D. R., Babu, K., Braverman, A. J., Eastwood, M. L., Green, R. O., Hobbs, J. M., Jewell, J. B., Kindel, B., Massie, S., Mishra,
M., et al.: Optimal estimation of spectral surface reflectance in challenging atmospheres, Remote Sensing of Environment, 232, 111 258,
2019.

Thompson, D. R., Braverman, A., Brodrick, P. G., Candela, A., Carmon, N., Clark, R. N., Connelly, D., Green, R. O., Kokaly,
R. F., Li, L., Mahowald, N., Miller, R. L., Okin, G. S., Painter, T. H., Swayze, G. A., Turmon, M., Susilouto, J., and Wettergreen, D. S.: Quantifying uncertainty for remote spectroscopy of surface composition, Remote Sensing of Environment, 247,
https://doi.org/https://doi.org/10.1016/j.rse.2020.111898, 2020.